Interaction between a cavitation bubble and shear flow

SADEGH DABIRI[1], WILLIAM A. SIRIGNANO[1]†
AND DANIEL D. JOSEPH[1,2]

[1]Department of Mechanical and Aerospace Engineering, University of California, Irvine, CA 92697, USA

[2]Department of Aerospace Engineering and Mechanics, University of Minnesota, Minneapolis, MN 55455, USA

The deformation of a cavitation bubble in shear and extensional flows is studied numerically. The Navier–Stokes equations are solved to observe the three-dimensional behaviour of the bubble as it grows and collapses. During the collapse phase of the bubble, two re-entrant jets are observed on two sides of the bubble. The re-entrant jets are not the result of interaction with a solid wall or free surface; rather, they are formed due to interaction of the bubble with the background flow. Effects of the viscosity, surface tension and shear rate on the formation and strength of re-entrant jets are investigated. Re-entrant jets with enough strength break up the bubble into smaller bubbles. Post-processing and analysis of the results are done to cast the disturbance by the bubble on the liquid velocity field in terms of spherical harmonics. It is found that quadrupole moments are created in addition to the monopole source.

1. Introduction

Cavitation occurs in many applications, such as liquid injectors, propellers and valves. Specifically, it is more common that cavitation inception occurs near or on solid boundaries (Brennen 1995). This is due to the pressure drop caused by rapid change in the flow direction. In addition, on these surfaces, inside the boundary layers, high levels of shear stress are present, which may lead to a stress-induced cavitation (Joseph 1998; Dabiri, Sirignano & Joseph 2007). In some cases, such as liquid injectors with sharp inlet corners, the boundary layer separates from the wall right behind the sharp corner. Therefore, it is of interest to study the interaction of cavitation bubbles with a shear flow.

Dynamics of asymmetrical cavitation bubbles have been under investigation for a long time. Most notably, cavitation bubbles near solid boundaries have been studied by many researchers (Lauterborn & Bolle 1975; Blake & Gibson 1987). However, most of the numerical studies are limited to the boundary element method. This is mainly due to the advantage this method offers in reducing the dimensions of the problem by one. However, the drawback is that the method is limited to either irrotational flows or Stokes flows. Therefore, the case of a rotational flow at finite Reynolds number cannot be studied by this method.

† Email address for correspondence: sirignan@uci.edu

Navier–Stokes solutions of cavitation bubbles are very limited. Popinet & Zaleski (2002) studied the effects of viscosity on creation of re-entrant jets during collapse of a cavitation bubble near a rigid boundary. They have solved the Navier–Stokes equations in an axisymmetric problem and have showed that large viscosity prevents jet impact inside the bubble. Yu, Ceccio & Tryggvason (1995) also examined solutions of Navier–Stokes equations for a bubble in viscous liquids. They considered the collapse of a bubble in a shear flow near a rigid wall to simulate the condition of cavitation bubbles inside a wall boundary layer. They found that, if the shear rate is large enough, the creation of the re-entrant jets will be suppressed.

To study the deformation of bubbles in shear flow, a fundamental problem has been considered here. A spherical bubble is placed initially in a simple shear flow and/or extensional flow; pressure drops for half a cycle and, in the next half cycle, recovers to its initial value. During this time, the bubble grows as it deforms due to strain in the flow. Then, as the pressure recovers, the bubble collapses and rebounds.

In the next section, governing equations and numerical methods are explained. Then, a benchmark problem is presented to validate the code and finally, results of the bubble dynamics are presented and discussed.

2. Governing equations

We consider the deformation of a cavitation bubble in a viscous liquid. The governing equations for this three-dimensional problem follow:

$$\rho_i \left(\frac{\partial \boldsymbol{u}}{\partial t} + \boldsymbol{u} \cdot \nabla \boldsymbol{u} \right) = -\nabla p + \nabla \cdot \boldsymbol{T} + \sigma \kappa \delta(d) \boldsymbol{n}, \tag{2.1}$$

where $\boldsymbol{u}$, ρ and μ are the velocity, density and viscosity of the fluid, respectively. Subscript i could represent either liquid (l) or gas (g) phase and $\boldsymbol{T}$ is the viscous stress tensor. The last term represents the surface tension as a force concentrated on the interface. Here, σ is the surface tension coefficient, κ is twice the local mean curvature of the interface, δ is the Dirac delta function, d represents the distance from the interface and $\boldsymbol{n}$ corresponds to the unit vector normal to the interface. The continuity equation for the liquid is

$$\nabla \cdot \boldsymbol{u} = 0 \tag{2.2}$$

and for the gas inside the bubble

$$\nabla \cdot \boldsymbol{u} = -\frac{1}{\rho} \frac{\mathrm{D}\rho}{\mathrm{D}t}. \tag{2.3}$$

The bubble is assumed to consist of a non-condensable ideal gas going through a polytropic process, i.e. $p \propto \rho^n$, where n is the polytropic exponent. For the small bubbles and low frequencies of pressure variation, the process is closer to isothermal because the thermal diffusion time scale is smaller than the pressure variation time scale. On the other hand, for large bubbles and high frequencies, the process is closer to adiabatic. The value of n has been provided by Plesset & Prosperetti (1977) as a function of two dimensionless parameters. For lower frequencies, which is the case in this study, the value of n depends only on one of the parameters, $G = R_o^2 \omega / D_g$, where $\omega = 2\pi/T$ is the frequency and D_g is the thermal diffusivity of the gas. In this study, $G = O(1)$ and therefore the process can be considered isothermal ($n = 1$). The density

variation can be related to pressure variation as

$$\frac{1}{\rho}\frac{D\rho}{Dt} = \frac{1}{np}\frac{Dp}{Dt},$$ (2.4)

where D/Dt represents the Lagrangian derivative. We consider the cases where the collapse velocity of the bubble is much smaller than the speed of sound in the bubble and the bubble density can be assumed to be uniform. The value of this uniform density, $\overline{\rho_g}$, is related to the average pressure inside the bubble, $\overline{p_g}$, through the polytropic equation, $\overline{p_g} \propto \overline{\rho_g}^n$. By relating the bubble density to the average pressure inside the bubble instead of the local pressure, one can suppress propagation of acoustic waves inside the bubble. These waves occur on a time scale that is not of interest here. Therefore, the continuity equation for the gas phase is rewritten as

$$\nabla \cdot \boldsymbol{u} = -\frac{1}{n\overline{p_g}}\frac{d\overline{p_g}}{dt}$$ (2.5)

inside the bubble.

3. Numerical implementation

A finite-volume method on a staggered grid is used to discretize and find the numerical solution of the unsteady Navier–Stokes equations. The convective and advective terms are discretized using the QUICK scheme (Hayase, Humphrey & Greif 1992), and the SIMPLE algorithm, developed by Patankar (1980), is used to solve the pressure–velocity coupling. The time integration is accomplished using the second-order Crank–Nicolson scheme.

A level-set method is used to capture the interface and model the surface tension, which has been developed by Osher and coworkers (e.g. Sussman *et al.* 1998 and Osher & Fedkiw 2001). The level-set function, denoted by θ, is defined as a signed distance function. It has positive values in the gas phase and negative values in the liquid phase. The magnitude of the level set at each point in the computational field is equal to the distance from that point to the interface.

Time evolution of the level-set function is governed by

$$\frac{\partial \theta}{\partial t} + \boldsymbol{u} \cdot \nabla\theta = 0.$$ (3.1)

Using the level-set function, one can define the fluid properties as

$$\rho = \rho_l + (\rho_g - \rho_l)H_\epsilon(\theta),$$ (3.2)
$$\mu = \mu_l + (\mu_g - \mu_l)H_\epsilon(\theta),$$ (3.3)

where subscripts l, g correspond to liquid and gas, respectively. H_ϵ is a smoothed Heaviside function defined as

$$H_\epsilon = \begin{cases} 0 & \theta < -\epsilon, \\ (\theta + \epsilon)/(2\epsilon) + \sin(\pi\theta/\epsilon)/(2\pi) & |\theta| \leqslant \epsilon, \\ 1 & \theta > \epsilon, \end{cases}$$ (3.4)

where ϵ represents the half-thickness of the interface, and has been given the value of 1.5 times the grid spacing. Using the definition of the Heaviside function, one can combine the continuity equations for liquid and gas phases (see (2.2) and (2.5)) into

one equation:

$$\nabla \cdot \boldsymbol{u} = -\frac{1}{n\bar{p}_g}\frac{\mathrm{d}\bar{p}_g}{\mathrm{d}t}H_\epsilon(\theta). \tag{3.5}$$

This single equation treats the gas inside the bubble as a compressible phase and the liquid as an incompressible phase.

4. Spherical cavitation bubble

In order to check the accuracy of the code, a comparison is made with the solution of spherical bubble growth and collapse. The radius of the bubble, R, is governed by the Rayleigh–Plesset–Poritsky (RPP) equation (Plesset & Prosperetti 1977):

$$R\ddot{R} + \frac{3}{2}\dot{R}^2 = \frac{1}{\rho_l}\left\{P_g - P_\infty - \frac{2\sigma}{R} - \frac{4\mu_l}{R}\dot{R}\right\}, \tag{4.1}$$

where P_∞ is the pressure at infinity, and P_g is the pressure inside the bubble at the interface and is related to the bubble volume through a polytropic equation $P_g = P_o(R_o/R)^{3n}$, where P_o is the pressure inside the bubble at the initial equilibrium radius, R_o. The bubble is initially at equilibrium and starts to grow, collapse and rebound as the pressure varies. The pressure variation is given by

$$P_\infty = \begin{cases} P_{o\infty} - \frac{\Delta P}{2}[1 - \cos(2\pi\frac{t}{T})] & t < T, \\ P_{o\infty} & T \geqslant t. \end{cases} \tag{4.2}$$

Using the initial radius of the bubble, R_o, as the length scale and $R_o\sqrt{\rho_l/P_{o\infty}}$ as the time scale, one can derive the dimensionless form of the RPP equation as

$$R^\star\ddot{R}^\star + \frac{3}{2}\dot{R}^{\star 2} = P_g^\star - P_\infty^\star - \frac{2}{We_p}\frac{1}{R^\star} - \frac{4}{Re_p}\frac{\dot{R}^\star}{R^\star}, \tag{4.3}$$

where Reynolds number, Weber number and dimensionless pressures are defined as

$$Re_p = \frac{R_o\sqrt{\rho_l P_{o\infty}}}{\mu_l}, \quad We_p = \frac{R_o P_{o\infty}}{\sigma}, \quad P_g^\star = \frac{P_g}{P_{o\infty}}, \quad P_\infty^\star = \frac{P_\infty}{P_{o\infty}}. \tag{4.4}$$

A three-dimensional calculation is performed, in which the centre of mass of the bubble is placed at the origin initially and stays there due to symmetry. Also, due to spherical symmetry in the problem, only one eighth of the domain is solved on a Cartesian grid with symmetrical boundary conditions on x–y, y–z and x–z planes. On the three other faces of the computational domain, time-varying pressure is applied. Since the boundaries of the domain are at finite distance, pressure from the solution of the RPP equation is calculated at the position of the boundary and applied as the pressure boundary condition.

The computational domain consists of 50^3 grid points with 10 grids across the initial radius of the bubble. Figure 1 shows the pressure variation and the resulting radius of the bubble predicted by the RPP equation and the Navier–Stokes solution. Dimensionless parameters are $Re_p = 70.71$, $We_p = 500$, $(\Delta P)/(P_{o\infty}) = 0.8$, $T^\star = 7.071$.

5. Bubble in shear or extensional flows without pressure variation

We are interested in the interaction of the cavitation bubbles with a simple shear flow. Therefore, we initially considered an incompressible bubble in a simple shear flow, $\boldsymbol{u} = k_s y\hat{\boldsymbol{x}}$. The bubble is placed at the centre of cubical domain. Due to symmetry
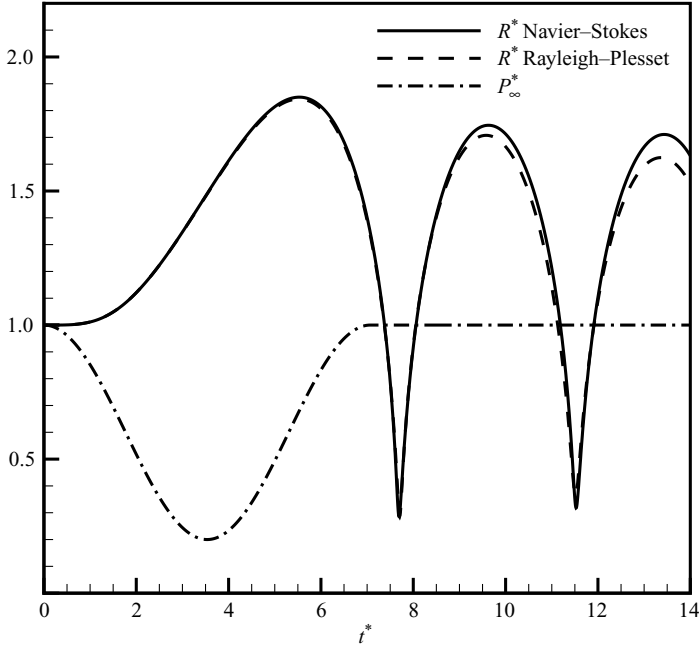
FIGURE 1. Radius of a spherical bubble and the applied pressure.

around the x–y plane and anti-symmetry around the x–z plane, only one quarter of the cubical computational domain is solved. The symmetry and anti-symmetry conditions also imply that the centre of the bubble will remain at the origin. The boundary conditions are as follows: on the $x = x_{min}$ plane, a linear profile for x-component of velocity, $u = k_s y$, is specified; on the $y = y_{max}$ plane, a constant x-component of velocity, $u = k_s y_{max}$, is specified. On the $y = 0$ plane, an antisymmetric boundary condition is applied, which is extracted from the following conditions:

$$u(-x, -y, z) = -u(x, y, z), \qquad (5.1)$$
$$v(-x, -y, z) = -v(x, y, z), \qquad (5.2)$$
$$w(-x, -y, z) = w(x, y, z). \qquad (5.3)$$

All other velocities have zero gradients in the direction normal to the boundaries.

For this problem, a different set of Reynolds number and Weber number can be defined based on shear rate or normal strain rate times the initial radius of the bubble as the velocity scale:

$$Re_s = \frac{\rho_l k R_o^2}{\mu_l}, \qquad We_s = \frac{\rho_l k^2 R_o^3}{\sigma}, \qquad (5.4)$$

where k represents the shear rate and/or the normal strain rate. The steady shape of the bubble and velocity field for $Re_s = 1$ and $We_s = 0.05$ are shown in figure 2. The deformation factor D (difference between long and short axes of the bubble divided by their summation) at steady state for the simple shear cases is 0.0489. For a small capillary number, $Ca = (We_s)/(Re_s) = (\mu_l k R_o)/\sigma$, the steady state value of the deformation parameter is almost equal to capillary number, i.e. $D \cong Ca$. The difference between current numerical results with experiments (e.g. Rust & Manga 2002) falls within the range of experimental uncertainty. Two circulating regions which are driven by the shear on the surface of the bubble are observed inside the
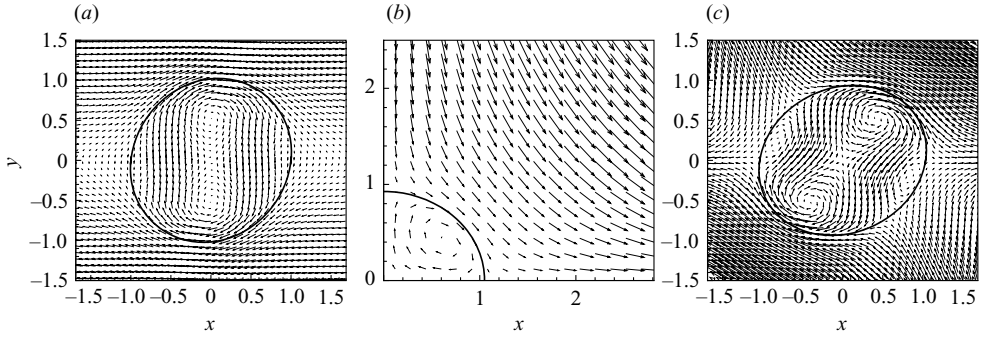
FIGURE 2. Steady shape of an incompressible bubble at $Re_s = 1$. $We_s = 0.05$ in (*a*) simple shear flow, (*b*) normal-strain flow and (*c*) combined flow.
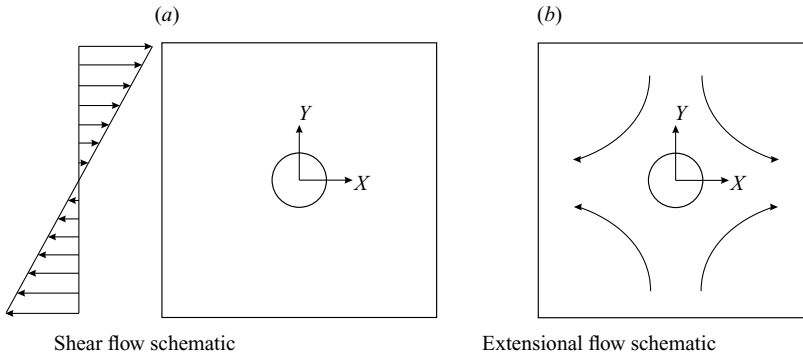

FIGURE 3. Schematics of shear and extensional flows. An initially spherical bubble is shown at the centre of the computational domain in addition to the far-field flow conditions.

bubble. These regions, which appear on top and bottom of the bubble, have the same vorticity direction as the simple shear flow.

Similar calculations are performed with normal strain and combined shear and normal strains in the background flow. The strain rates are k_s and k_n and have the same value as k_s in the simple shear flow case. Results are shown in figure 2. Two similar recirculation regions formed in the simple shear flow are also present in the cases with combined shear and normal strain flows. In addition, two smaller regions of recirculating flow can be seen inside the bubble on the left and right, which have vorticities opposite of the two larger vortices and the background flow.

6. Cavitation bubble with sinusoidal pressure variation interacting with shear or extensional flows

In this section, a cavitation bubble in simple shear flow, a normal strain flow or a combination of these flows is again considered. However, now the pressure will vary with time. A schematic of the problem is shown in figure 3. The bubble is initially spherical and is located at the origin. The initial velocity field is specified as $\boldsymbol{u} = k_s y \hat{\boldsymbol{x}}$ for shear flow, $\boldsymbol{u} = k_n x \hat{\boldsymbol{x}} - k_n y \hat{\boldsymbol{y}}$ for extensional flow or $\boldsymbol{u} = (k_s y + k_n x) \hat{\boldsymbol{x}} - k_n y \hat{\boldsymbol{y}}$ for a combined shear and extensional flow. The boundary conditions for shear flow are the same as explained in §5, except that on $x = x_{min}$, a zero normal gradient is applied instead of applying a linear velocity profile. The reason for this change is that in the

Case	Re_s	We_s	Re_p	We_p	$k^\star$	$T^\star$	$\Delta P^\star$	Flow type
1	0	0	70.71	500	0	7.071	0.8	Stagnant
2	2.5	0.625	70.71	500	0.03535	7.071	0.8	Shear
3	5.0	2.5	70.71	500	0.07071	7.071	0.8	Shear
4	7.5	5.624	70.71	500	0.10606	7.071	0.8	Shear
5	10.0	10.0	70.71	500	0.1414	7.071	0.8	Shear
6	5	0.3535	70.71	25	0.07071	7.071	0.8	Shear
7	1.0	0.05	14	9.8	0.07143	21	0.9796	Shear
8	1.0	0.05	14	9.8	0.07143	21	0.9796	Normal strain
9	1.0	0.05	14	9.8	0.07143	21	0.9796	Combined
10	4	0.2667	40	26.67	0.1	30	0.99	Shear

TABLE 1. List of parameters for cavitation bubble in strained flow.

case of the compressible bubble, the bubble volume will change with time. This will create a net out-flux or in-flux on the domain. To allow this flux to be distributed over all the surfaces of the computational domain, a Neumann boundary condition is needed rather than a Dirichlet boundary condition. Dimensionless parameters are the same as in §4. In addition, the strain rate, k, either shear or normal, is provided in a dimensionless form as

$$k^\star = kR_o\sqrt{\frac{\rho_l}{P_{o\infty}}}. \tag{6.1}$$

Table 1 shows a list of dimensionless parameters for the cavitation bubble and the type of the background flow. Unlike the spherical cavitation bubble in stagnant flow (§4), where the pressure on boundaries can be calculated from the RPP equation, in the strained flow, the pressure on the boundary cannot be calculated having only the value of pressure at infinity. Therefore, in this section, the pressure profile shown in figure 1 is applied directly on the boundary. To assess the effects of this change in the boundary conditions, volume of the bubble is plotted for two cases in figure 4. The dashed line in figure 4(*a*) represents the case where the boundary condition for pressure is calculated from the RPP solution; this is, in fact, the same calculation as showed in §4. The solid line represents the solution where the pressure is applied directly on the boundary (Case 1). Of course, there are differences between these two solutions. Case 1 has a larger value of the maximum volume. Since, in this case, the pressure is applied on the boundary at a finite distance from the bubble, both the pressure gradient outside the bubble and the rate of growth of the bubble will be larger. Whereas, for the other case, the pressure variation is applied at infinity and the pressure value on the boundary is extracted from the solution of the RPP equation. The other difference is in the period of oscillation, which is smaller for Case 1. Similarly, this can be explained by considering the boundary conditions. Since the accelerated mass between the bubble surface and the boundary is smaller than the accelerated mass between bubble surface and infinity, and the period of oscillation increases with the mass, one should expect a larger period for Case 1 compared to results of §4. In another explanation, the boundary condition from the RPP equations results in a smaller pressure gradient over similar domains. This causes a smaller acceleration of liquid, and therefore, a longer period of oscillation for the RPP solution.

In figure 4(*b*), the volume of the bubble is shown for Cases 1–5. Note that for these five cases, all the parameters are the same and only the shear rate is changed. As it
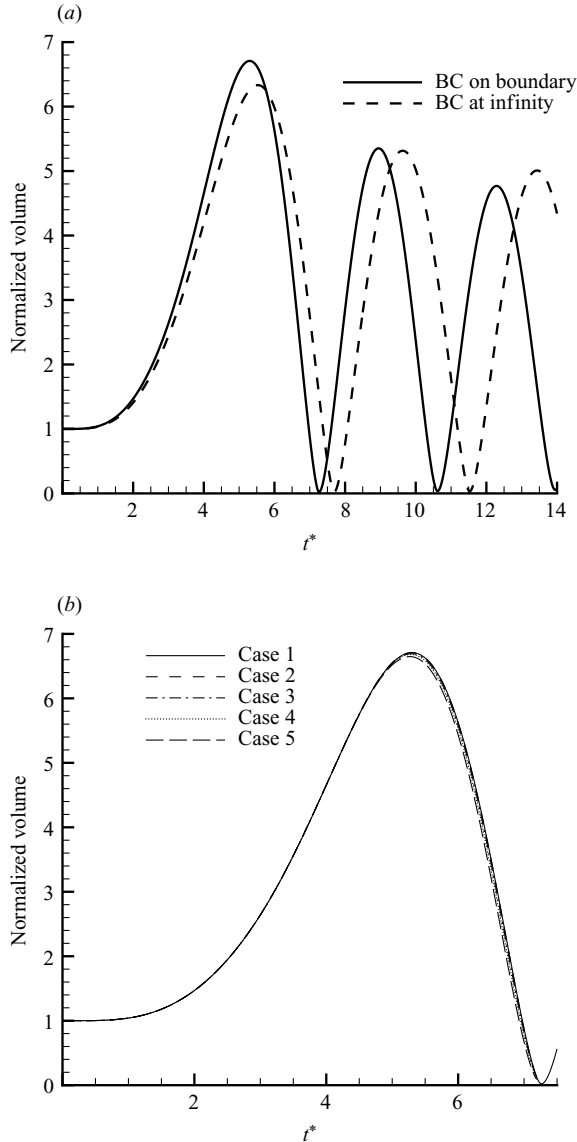
FIGURE 4. (*a*) Effect of boundary condition on volume of a spherical cavitation bubble in a stagnant liquid; pressure variation applied directly on the boundary (solid line) and pressure variation from the RPP solution (dashed line). (*b*) Effects of the shear on the bubble volume.

can be seen in figure 4, the shear rate has a negligible influence on the volume of the bubble. Still, it can be observed that the increase in the shear rate slightly suppresses the growth of the bubble.

Figure 5 shows snapshots of the cavitation bubble from the instant it reaches its maximum volume until it collapses for Case 3. Figure 5(*a*) shows the bubble at its maximum volume. This maximum volume occurs slightly after the pressure reaches its minimum and starts to recover. This is due to the inertia of the liquid. At the maximum volume, the bubble has an ellipsoidal shape, which is a result of the shear
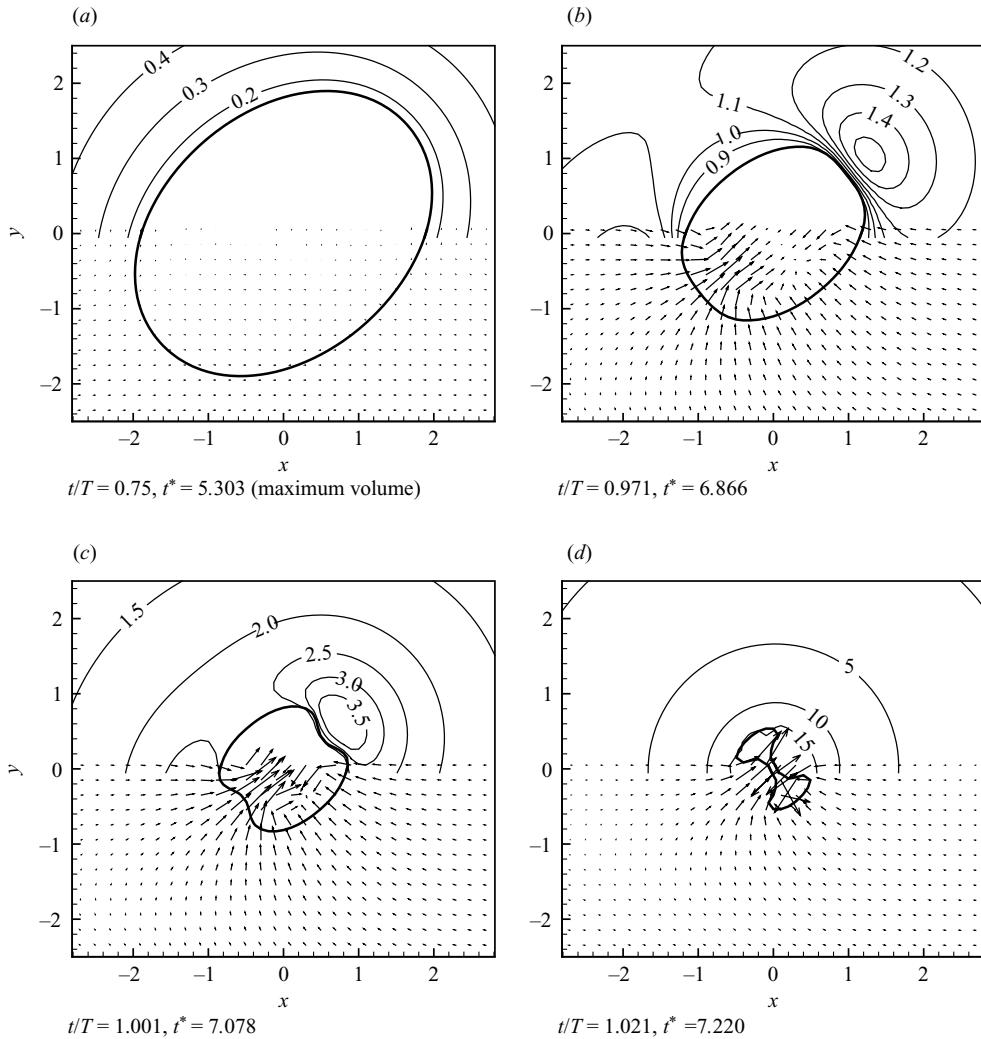
FIGURE 5. Pressure contours and velocity field during collapse of cavitation bubble in shear flow for Case 3.

flow. As the bubble collapses, two regions of high pressure are formed on upper right and lower left sides of the bubble. These high pressure regions later lead to the creation of two flat regions, and later concave regions, on the surface of the bubble. This finally results in the formation of two re-entrant jets on the sides of the bubble.

The shapes of the bubbles for Cases 1–5 are shown side by side in figure 6. The large deformation of the bubbles can be explained by considering the Weber number. Since in these calculations the Weber number, We_p, is relatively large, the surface tension is not strong enough to keep the bubble in a spherical shape.

As expected, the deformation of the bubble from a spherical shape at its maximum volume is larger for cases with higher shear rate. Also, two re-entrant jets are formed on the two sides of the bubble.
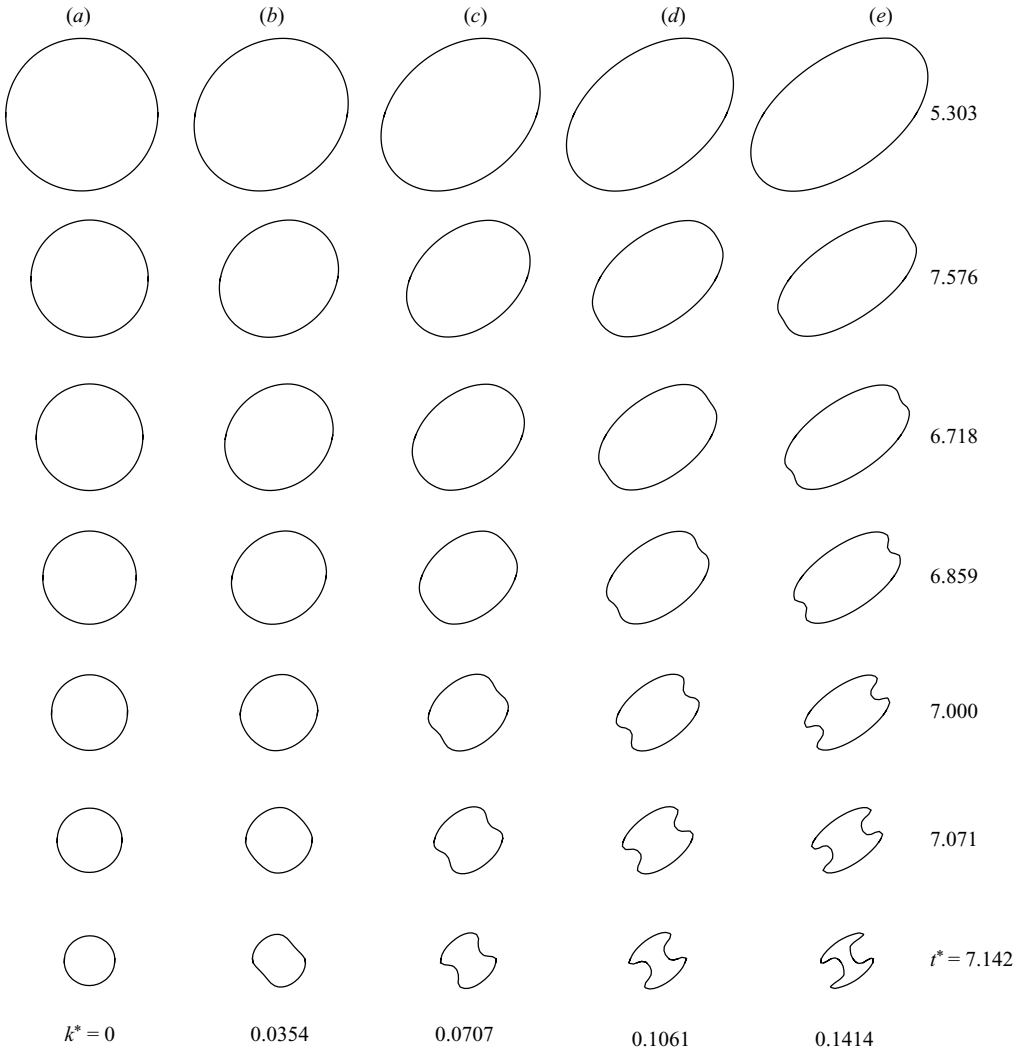
FIGURE 6. Effect of shear on the bubbles' shape during collapse. (a–e) $k^\star$ is the dimensionless shear rate increasing from left to right. Cross sections of the bubbles are shown at different instants of time from the instant of maximum volume on top until the collapse of the bubble on the bottom. $Re = 70.71$, $We = 500$.

The deformation of cavitation bubbles from the spherical shape has been quantified through calculation of a dimensionless surface to volume ratio for bubbles:

$$\text{surface-to-volume ratio} = \frac{A}{(6\sqrt{\pi}V)^{2/3}}, \qquad (6.2)$$

where A and V are the surface area and volume of the bubble, respectively. This is the surface-to-volume ratio normalized by the surface-to-volume ratio of a sphere with the same volume. Therefore, a spherical bubble will always have a dimensionless surface-to-volume ratio of one, and as the bubble deviates from spherical shape, this value increases. Figure 7 shows the surface-to-volume ratio as a function of
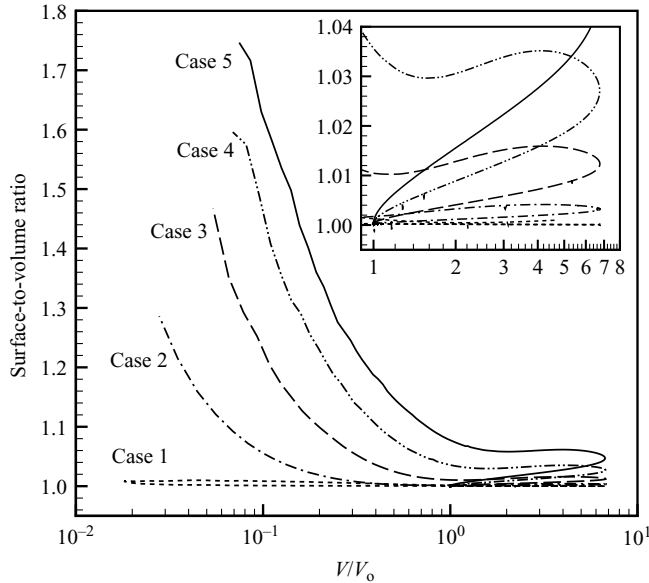
FIGURE 7. Non-dimensional surface-to-volume ratio vs. bubble volume for Cases 1–5.

dimensionless volume of the bubble for Cases 1–5. As can be seen, the deformation of the bubble increases with the shear rate and it has the largest value during the collapse of the bubble for each case. Ideally, one expects Case 1 to have a constant value of surface-to-volume ratio of one.

Surface tension effects are studied by considering Case 6, which is similar to Case 3, but with larger surface tension. In this case, the bubble deformation is very similar to Case 3. However, the collapse occurs earlier than Case 3. Since the pressure drop across the interface is larger than Case 3, both the pressure difference in the liquid and the growth rate of the bubble have to be smaller. The shape of the bubble during collapse and rebound is shown in figure 8. It can be seen that the re-entrant jets collide and create a hole in the bubble. However, in this case, the bubble does not break up.

The calculation for Case 6 is also performed on a finer grid of $200 \times 100 \times 100$ grid points and results are compared to the case with regular grid of $100 \times 50 \times 50$ grid points in figure 9. The cross-section of the bubble in two calculations match with each other closely. Also, another calculation is performed with a smaller time step to ensure the sufficiency of time resolution (figure 9). The dependency of the solution on the size of the computational domain is checked by increasing the domain size by 50 % in each direction and keeping the grid spacing fixed. This change in the size of computational domain caused a 1 % increase in the maximum volume of the cavitation bubble.

Another case is shown in figure 10, which refers to lower Reynolds number and Weber number. Even though re-entrant jets are formed in these cases, they do not impinge on each other due to the strong surface tension. Note that the values of Reynolds and Weber numbers based on the shear, Re_s, We_s, for this case are the same as one of the calculations for incompressible bubble in shear flow in §5. By comparing the results with the incompressible bubble in shear flow, one can observe that the shear flow does not deform the bubble severely. Moreover, the pressure change alone, which results in the growth and collapse of the bubble, does not cause

(a) $t/T = 0.830$, $t^* = 5.869$ (b) $t/T = 0.950$, $t^* = 6.718$ (c) $t/T = 1.0$, $t^* = 7.071$

(d) $t/T = 1.014$, $t^* = 7.170$ (e) $t/T = 1.038$, $t^* = 7.340$ (f) $t/T = 1.086$, $t^* = 7.679$
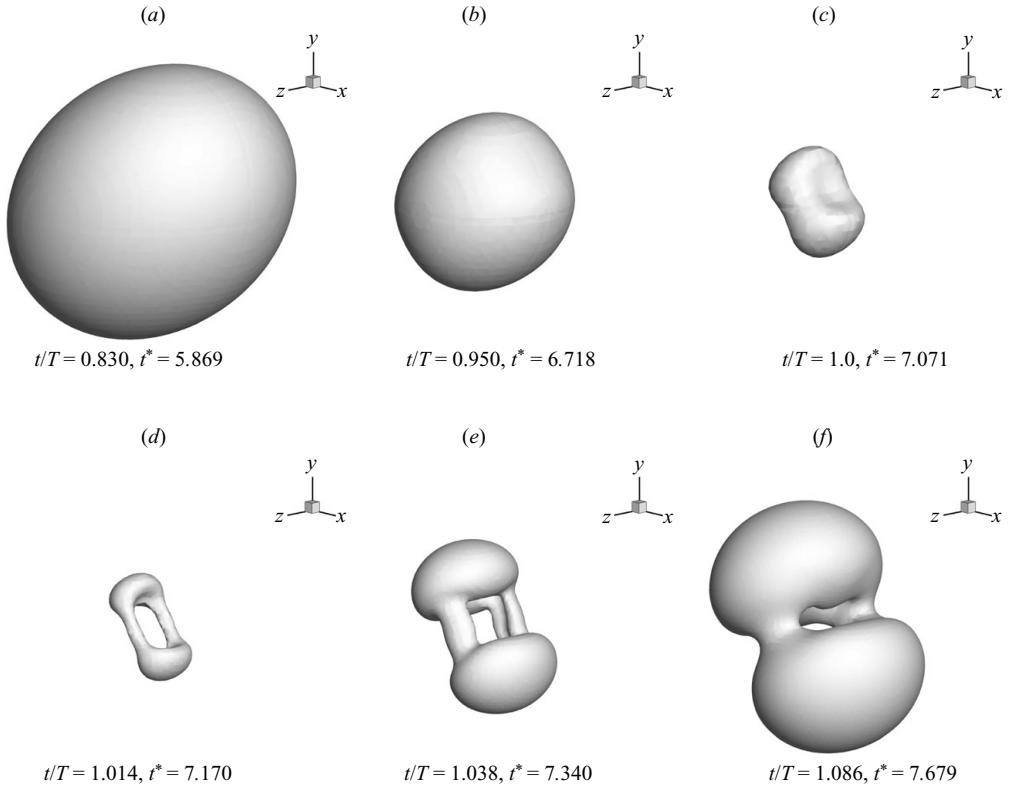
FIGURE 8. Shape of the bubble during collapse and rebound for Case 6. Creation and impingement of re-entrant jets results in the formation of a hole inside the bubble.
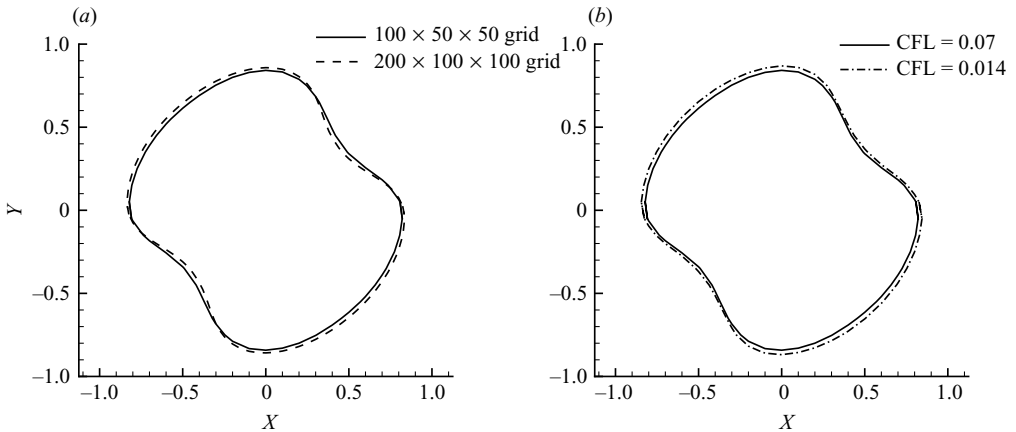

FIGURE 9. Grid independency and time-step independency tests for Case 6. (a) Cross-section of the bubble on a regular $100 \times 50 \times 50$ gird and a finer $200 \times 100 \times 100$ grid. (b) Cross-section of the bubble from two simulations with different time steps, CFL = 0.07, CFL = 0.014. $t^* = 6.972$, $t/T = 0.986$.
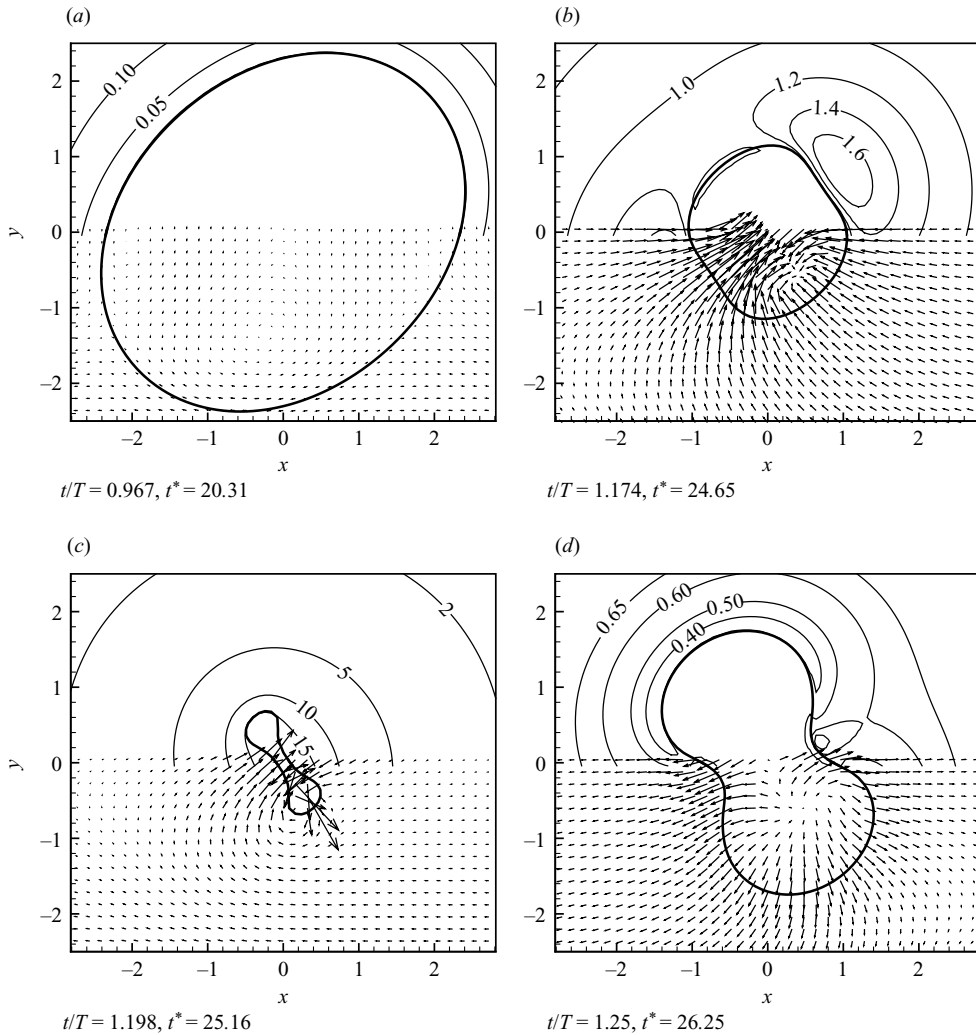
FIGURE 10. Collapse of cavitation bubble in shear flow for Case 7. Bubble interface, velocity vectors and pressure coefficient contours are shown in the plane of symmetry of the bubble.

any deviation from the spherical shape of the bubble. Therefore, it is the combined effect of shear and pressure variation that results in such a large deviation from spherical shape.

In Case 10, shown in figure 11, the impingement of re-entrant jets results in the break-up of the bubble. First, a hole is created inside the bubble and then the gas threads, connecting the top and bottom of the bubble, break up and create satellite bubbles.

It can be seen that the break-up of the cavitation bubble is essentially different from the break-up of a non-cavitating (i.e. incompressible) bubble. In the case of an incompressible bubble, the bubble stretches in the direction of principal stress, i.e. 45°from the velocity for small deformations. However, in our case, the bubble initially extends in the same direction as an incompressible bubble, but during the collapse the bubble retracts and the re-entrant jets form. In the break-up of an incompressible bubble, the capillary effects cause the necking and break-up of the bubble after it
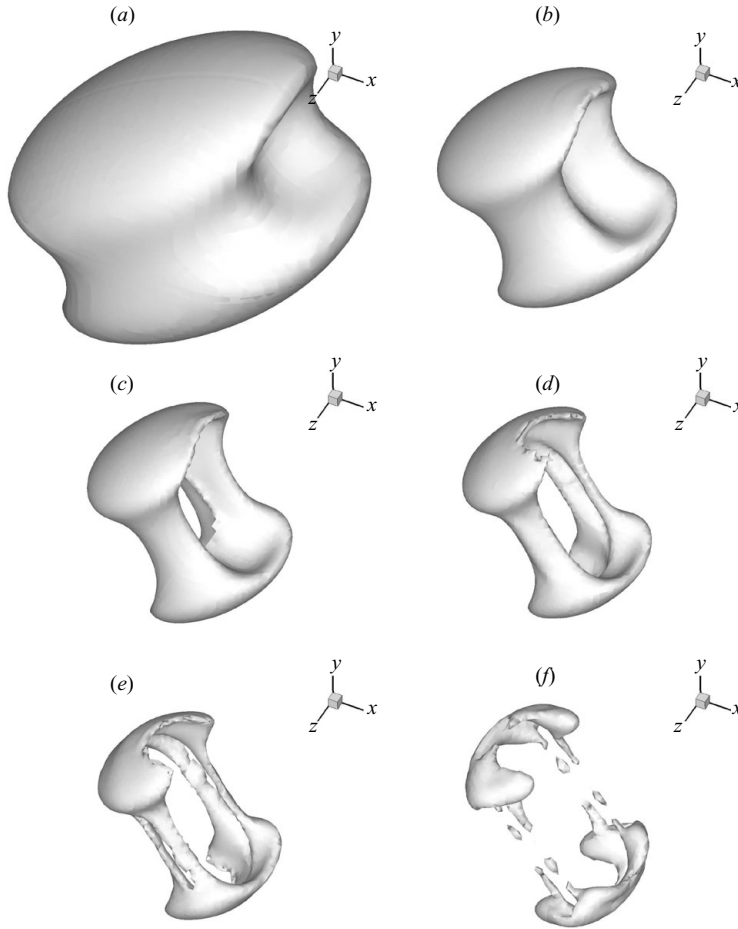
FIGURE 11. Shape of the bubble during collapse and rebound for Case 10. Creation and impingement of re-entrant jets results in the break-up of the bubble. $t^* = 68.13$ (*a*); 68.78 (*b*); 68.95 (*c*); 69.03 (*d*); 69.07 (*e*); 69.16 (*f*).

has been stretched by the shear in the flow. Whereas, here, the capillary phenomenon does not play an important role in the break-up process. It is rather the inertia of the re-entrant jets that breaks up the bubble. Still one can say that the capillary effects become important in the break-up of the gas threads that are formed after the re-entrant jets collide.

A case with a normal strain rate has also been considered. Figure 12 shows the shape of the bubble from the instance of its maximum volume until its collapse and rebound. This case has flow parameters similar to Case 7. However, the background flow is extensional ($\boldsymbol{u} = kx\hat{\boldsymbol{x}} - ky\hat{\boldsymbol{y}}$), with magnitude of the strain rate same as in Case 7. In this case, the bubble deforms during growth phase and elongates in the x direction. During the collapse of the bubble, a high pressure region is formed on the right (and left due to symmetry) side of the bubble and re-entrant jets are formed.

Case 9 has the combined shear and normal strain flow in the background. Figure 13 shows the shape of the bubble for this case. High pressure zones and re-entrant jets are still formed.
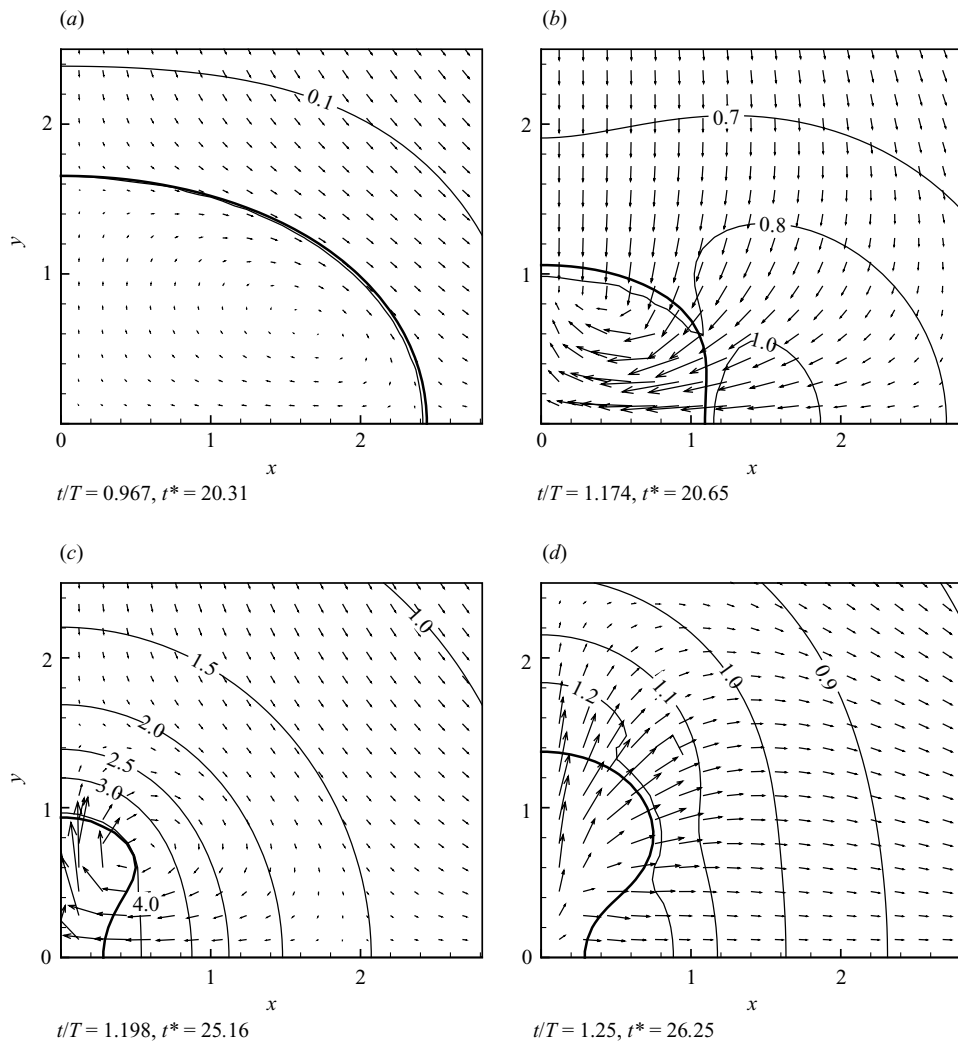
FIGURE 12. Collapse of cavitation bubble in a flow with normal strain for Case 8. Bubble interface, velocity vectors and pressure coefficient contours are shown in the plane of symmetry of the bubble.

7. Vorticity generation at bubble interface

In this section, the vorticity field around the bubble is studied. Figure 14 shows the z-component of the vorticity, ω_z, in the plane of symmetry of the bubble for Case 3.

Figure 15 shows the circulation integrals on the plane of symmetry of the bubbles for Cases 1–5. Circulation is calculated in a region of $-2.5 < x < 2.5$, $-2.3 < y < 2.3$ and it is divided into a positive and negative part as

$$\Gamma^{+} = \int \max(\omega_z^{\star} + k_s^{\star}, 0)\,\mathrm{d}x\,\mathrm{d}y, \quad \Gamma^{-} = \int -\min(\omega_z^{\star} + k_s^{\star}, 0)\,\mathrm{d}x\,\mathrm{d}y. \quad (7.1)$$

Note that $-k_s$ is the vorticity of the background flow and is subtracted from the vorticity in the above integral calculation. The vorticity, ω_z, has been non-dimensionalized in the same way as the shear rate. As it can be seen in this figure,
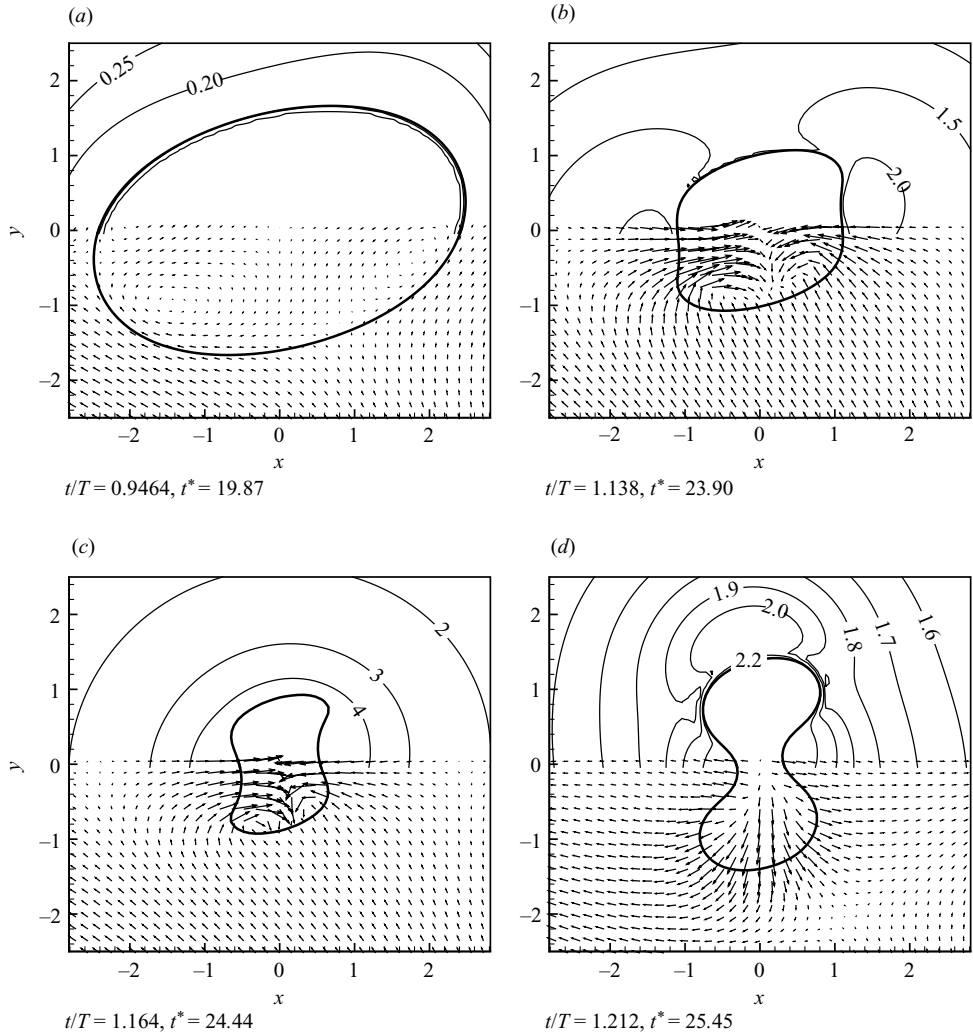
FIGURE 13. Collapse of cavitation bubble in a flow with combined shear and normal strain for Case 9. Bubble interface, velocity vectors and pressure coefficient contours are shown in the plane of symmetry of the bubble.

vorticity generation increases with the shear rate in the flow. During the growth of the bubble, the positive part of the circulation integral, Γ^+, becomes larger than its negative part, which means the net change of circulation in the flow, $\Gamma^+ - \Gamma^-$, is positive and opposite of the circulation in the background flow. As the bubble starts to collapse, the difference between Γ^+ and Γ^- becomes less and later Γ^- exceeds Γ^+.

8. Spherical harmonics decomposition

Observing the velocity field near the bubbles during growth and collapse, we found that, in addition to monopole source or sink velocity field and a base shear flow, there exists a quadrupole velocity field that is produced by antisymmetrical
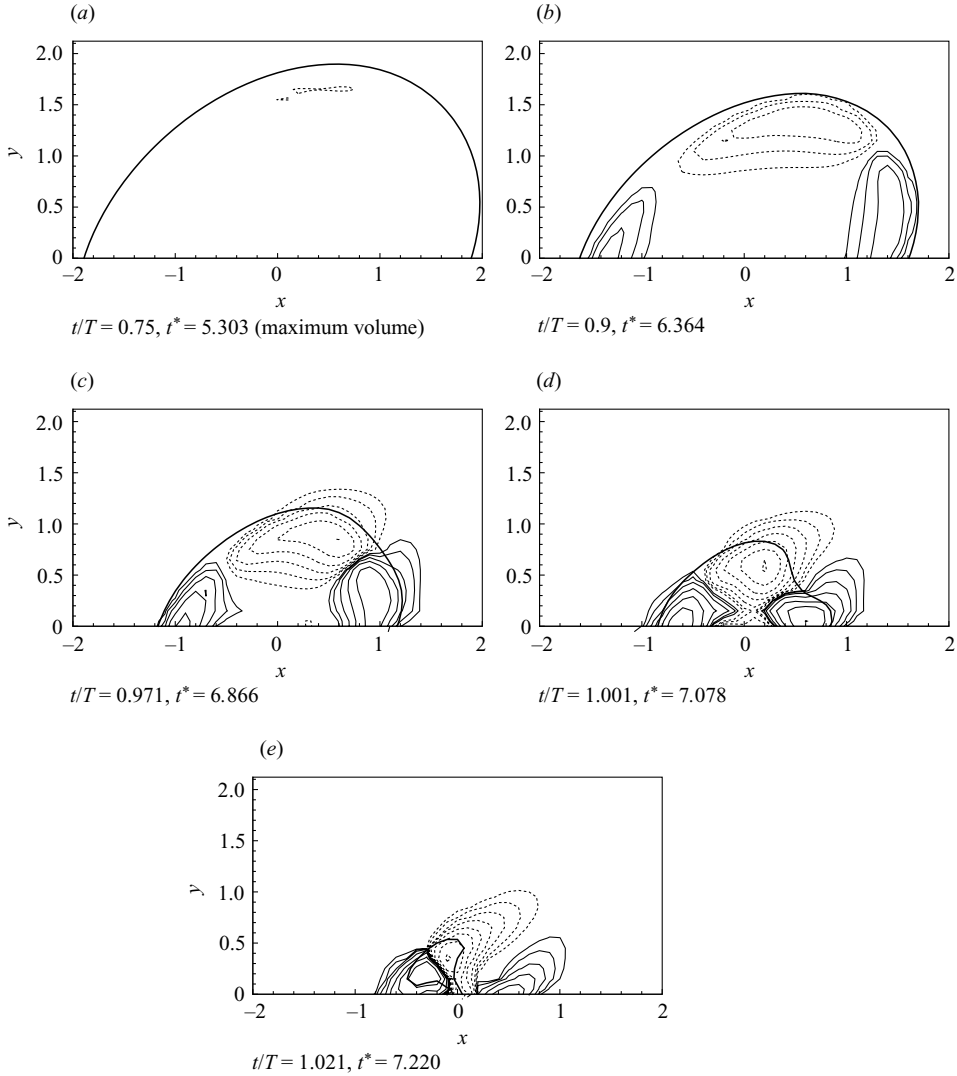
FIGURE 14. z-component of vorticity field during collapse of cavitation bubble in shear flow for Case 3. Vorticity levels are $\pm 4, \pm 8, \pm 16, \ldots$ times the vorticity of the base flow and negative-valued contours are dashed.

growth and collapse of the bubble. The velocity field can be expanded in terms of spherical harmonics to extract more information about the strength of monopole and quadrupole terms. The reason for using the spherical harmonics to expand the velocity field is based upon the physical interpretation of these harmonics. The zero-order harmonic represents a monopole, simple source or sink, in the flow which is created due to volume change of the bubble. The first-order harmonics represent dipoles, second-order harmonics represent quadrupoles and so on.

First, the background velocity is subtracted from the velocity field

$$\mathbf{u}' = \mathbf{u} - [(k_s y + k_n x)\hat{\mathbf{x}} - k_n y \hat{\mathbf{y}}]. \tag{8.1}$$
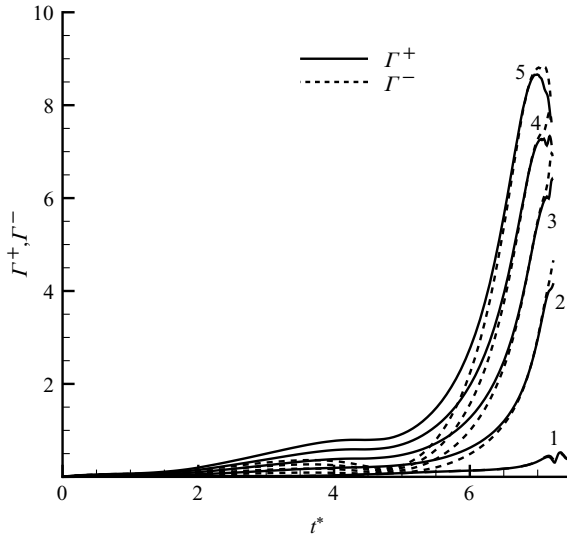
FIGURE 15. Vorticity integrals or circulation on the plane of symmetry of the bubbles for Cases 1–5.

Then, the radial component of the velocity field in spherical coordinates, with origin at the centre of the bubble, is expanded:

$$u'_r = \sum_{n,m} A_n^m(t,r) Y_n^m(\theta, \phi), \tag{8.2}$$

where Y_n^m's are the spherical harmonics, defined as

$$Y_n^m(\theta, \phi) = \sqrt{\frac{2n+1}{4\pi} \frac{(n-m)!}{(n+m)!}} P_n^m(\cos\theta) e^{im\phi}. \tag{8.3}$$

Since we are dealing with real numbers for velocity field, the complex exponential term in the harmonics is replaced by its real and imaginary parts and some of the coefficients are adjusted to make sure that the harmonics remain orthonormal.

Coefficients A_n^m in (8.2) can be found using

$$A_n^m(t,r) = \int u'_r Y_n^m(\theta, \phi) \, d\Omega \tag{8.4}$$

$$= \int_{\theta=0}^{\pi} \int_{\phi=0}^{2\pi} u'_r Y_n^m(\theta, \phi) \sin\theta \, d\theta \, d\phi, \tag{8.5}$$

where A_n^m is a function of $r^\star$ and time; we will consider the time dependency of the harmonics first. In a spherical coordinates with the origin placed at the centre of the bubble, the radial component of velocity is calculated at $r^\star = 2$. Then, the radial velocity is expanded in spherical harmonics to find coefficients A_n^m. Figure 16 shows coefficients of different harmonics as a function of time. Note that the first-order harmonics, representing dipoles, are zero due to the symmetry and antisymmetry conditions in the problem. The dipole is zero because the bubble is not accelerating relative to the liquid. The zero-order harmonic represents a monopole and can be
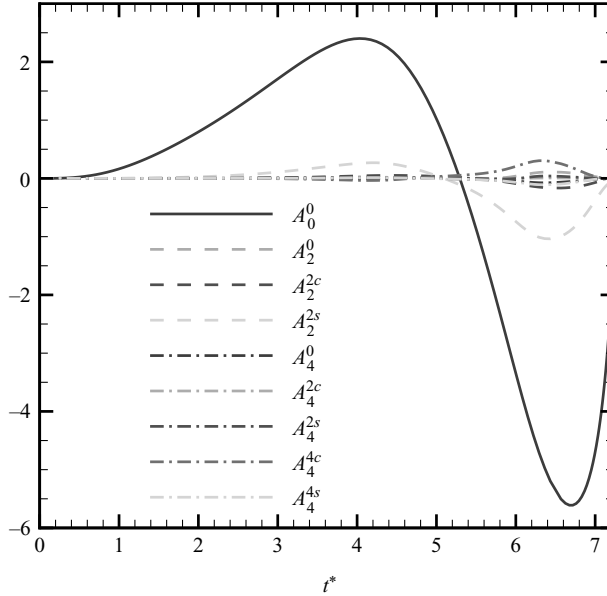
FIGURE 16. Coefficients of spherical harmonics in the velocity field at $r^\star = 2$ for Case 3. Solid line represents monopole, dashed lines represent quadrupole and dashed dot lines are for fourth-order harmonics.

related to the rate of volume change of the bubble:

$$\frac{\mathrm{d}V^\star}{\mathrm{d}t^\star} = \int r^{\star 2} u_r \, \mathrm{d}A = 2\sqrt{\pi} r^{\star 2} A_0^0. \tag{8.6}$$

Therefore, positive A_0^0 indicates growth and negative A_0^0 indicates collapse of the bubble. It can be seen that the monopole, A_0^0, is the dominant component in the spherical harmonics decomposition. The quadrupoles also have a strong contribution to the velocity field. Among the three non-zero harmonics of second order, A_2^{2s} is the largest one, which represents a quadrupole at 45° with x-axis, ($\phi = 45°$). As it can be seen, this moment correlates well with the monopole. During growth of the bubble, A_2^{2s} is positive indicating the stretch of the bubble in the direction of the shear. When the bubble is collapsing, A_2^{2s} becomes negative, which shows a faster collapse at $\phi = 45°$. This can be interpreted as a sign of the formation of re-entrant jets. The largest component of quadrupole always remains in the x–y plane, which is the plane of shear flow.

In order to visualize the contribution of different harmonics to the velocity field, the streamlines for Case 6 are shown in figure 17. In the first two images (a) and (b) the streamlines are shown at an instant of time during collapse of the bubble in the x–y plane and the x–z plane, respectively. Then, the base shear flow is subtracted from the velocity field and streamlines are plotted in (c). In the last part (d), the monopole is also subtracted from the velocity field. This velocity field consists of quadrupoles and higher-order harmonics.

Spherical harmonics decomposition is performed at different radii in order to determine the dependency of A_n^m on $r^\star$. The monopole term, A_0^0 is plotted at three different radii in figure 18. Then, the maximum absolute value of A_0^0 is plotted as a
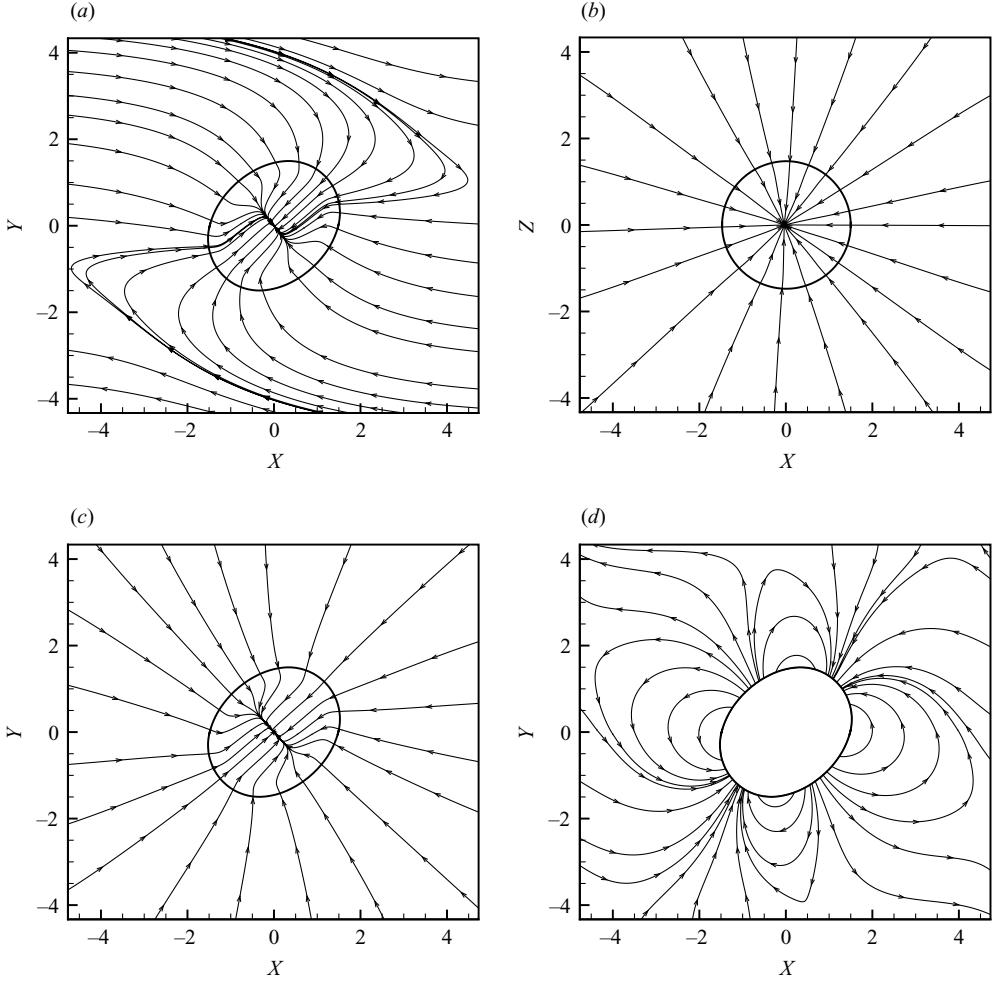
FIGURE 17. Streamlines during collapse of the bubble at $t^* = 6.505$ in Case 6: (*a*) streamlines from velocity field in the $z = 0$ plane, (*b*) $y = 0$ plane, (*c*) $z = 0$ plane after subtracting the base shear flow, (*d*) $z = 0$ plane after subtracting the base shear flow and monopole source.

function of $r^\star$ in figure 19 Fitting a power law to the data points, we find

$$A_0^0 \propto r^{\star -1.9985}. \tag{8.7}$$

One should expect this behaviour since it is a direct result of incompressibility of the liquid. The second-order harmonic A_2^{2s} is plotted at three different locations in figure 20 Two second-order harmonics A_2^{2s} and A_2^{2c} are merged into one using

$$A_2^2 = \sqrt{\left(A_2^{2s}\right)^2 + \left(A_2^{2c}\right)^2} \tag{8.8}$$

and are plotted versus $r^\star$ in figure 19 for Cases 2–5. As it can be seen, the monopole is the same for all four cases, which means that the shear rate does not affect the monopole strength. However, the quadrupole moment varies with the shear rate. Table 2 lists the equations for fitted power laws for quadrupole moments versus radius. The exponents are close to four, which is the theoretical value of the exponent for a velocity field due to a point quadrupole. Since the quadrupole is not applied
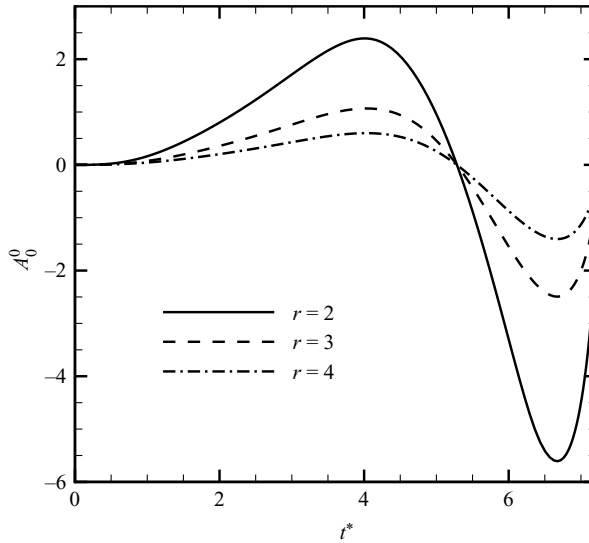
FIGURE 18. Monopole coefficient at different radii $r^\star = 2$, 3 and 4 for Case 3.
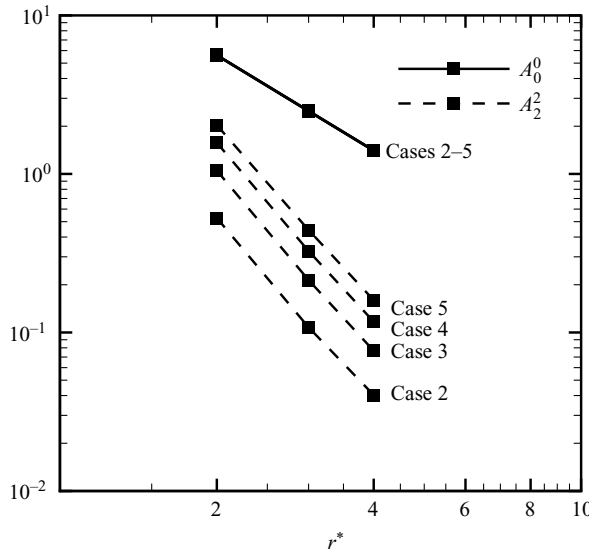

FIGURE 19. Dependency of harmonics on radius.

at a point here, and the surface of the sphere, on which the quadrupole moment is evaluated, is not very far from the bubble, a smaller absolute value of the exponent is expected. In addition, the velocity field is not irrotational, even after subtracting the base shear flow. The vorticity in the flow is not confined to the bubble, but rather it is distributed over the whole domain. For example, in Case 3, the magnitude of vorticity on the surface of a sphere at $r = 2$ reaches 39.6 % of the vorticity in the base flow. Therefore, we cannot expect to find a perfect quadrupole velocity field around the bubble. The average exponent for quadrupole term for Cases 2 to 5 is found to
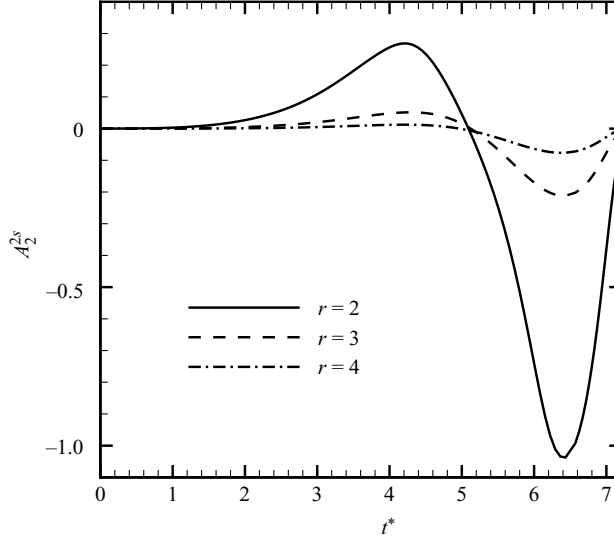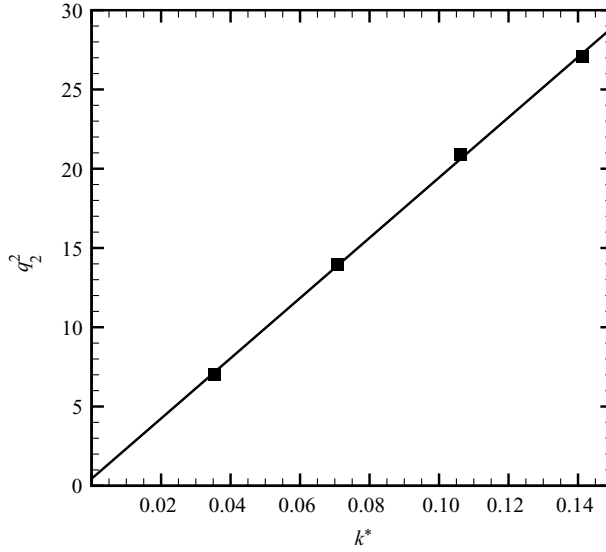
FIGURE 20. Coefficients of second-order harmonics at different radii for Case 3.

FIGURE 21. q_2^2 for different shear rates in the background flow.

be -3.736. Based on this average value, we define q_2^2 as

$$A_2^2 = \frac{q_2^2}{r^{\star -3.736}}. \tag{8.9}$$

Hence, q_2^2 is related to the quadrupole moment. Now, we can investigate the effect of shear rate in the background flow on the quadrupole moment. Figure 21 shows that the quadrupole moment is proportional to the shear rate in the flow.

Case	A_2^2
2	$6.811 r^{\star -3.724}$
3	$14.26 r^{\star -3.786}$
4	$21.01 r^{\star -3.760}$
5	$25.67 r^{\star -3.674}$

TABLE 2. Dependency of the quadrupole component of the velocity on $r^\star$.

9. Conclusion

In this paper, the deformation of a cavitation bubble due to the presence of a simple shear and/or extensional flow is investigated. The general approach is to understand the physics of the collapse of a cavitation bubble in shear flow. We are also interested in learning the ways in which the cavitation bubble affects the flow. The creation of a monopole and three quadrupoles is one way of influencing the flow; another method is by creating vorticity in the liquid phase. The deformation of the bubble in the direction of the background flow during growth results in the creation of high-pressure regions on sides of the bubble during the collapse. This leads to formation of re-entrant jets as the bubble collapses. Impingement of re-entrant jets inside the bubble results in the break-up of the bubble in some cases. The deformation of cavitation bubble with volume change is much larger than the incompressible bubble in the same flow environment. This suggests that the interaction between shear (or normal strain) flow and volume change is very important and can strongly change the behaviour of the cavitation bubble. A spherical harmonics decomposition of the velocity field near the bubble shows formation of quadrupoles during the collapse of the bubble. The strength of the quadrupoles are proportional to the strain rate in the background flow.

REFERENCES

BLAKE, J. R. & GIBSON, D. C. 1987 Cavitation bubbles near boundaries. *Annu. Rev. Fluid Mech.* **19**, 99–123.

BRENNEN, C. E. 1995 *Cavitation and Bubble Dynamics*. Oxford University Press.

DABIRI, S., SIRIGNANO, W. A. & JOSEPH, D. D. 2007 Cavitation in an orifice flow. *Phys. Fluids* **19** (7), 072112.

HAYASE, T., HUMPHREY, J. A. C. & GREIF, R. 1992 A consistently formulated quick scheme for fast and stable convergence using finite-volume iterative calculation procedure. *J. Comput. Phys.* **98**, 108–118.

JOSEPH, D. D. 1998 Cavitation and the state of stress in a flowing liquid. *J. Fluid Mech.* **366**, 367–376.

LAUTERBORN, W. & BOLLE, H. 1975 Experimental investigations of cavitation-bubble collapse in neighbourhood of a solid boundary. *J. Fluid Mech.* **72**, 391–399.

OSHER, S. & FEDKIW, R. P. 2001 Level set methods: an overview and some recent results. *J. Comput. Phys.* **169**, 436.

PATANKAR, S. V. 1980 *Numerical Heat Transfer and Fluid Flow*. Hemisphere.

PLESSET, M. S. & PROSPERETTI, A. 1977 Bubble dynamics and cavitation. *Annu. Rev. Fluid Mech.* **9**, 145–185.

POPINET, S. & ZALESKI, S. 2002 Bubble collapse near a solid boundary: a numerical study of the influence of viscosity. *J. Fluid Mech.* **464**, 137–163.

RUST, A. C. & MANGA, M. 2002 Bubble shapes and orientations in low Re simple shear flow. *J. Coll. Interface Sci.* **249** (2), 476–480.

SUSSMAN, M., FATEMI, E., SMEREKA, P. & OSHER, S. 1998 An improved level set method for incompressible two-phase flows. *Comput. Fluids* **27**, 663–680.

YU, P. W., CECCIO, L. & TRYGGVASON, G. 1995 The collapse of a cavitation bubble in shear flows: a numerical study. *Phys. Fluids* **7** (11).